Mathematics and Computers in Simulation 225 (2024) 528–544

Contents lists available at ScienceDirect

Mathematics and Computers in Simulation

journal homepage: www.elsevier.com/locate/matcom

Original articles

# Numerical simulation of 3D vorticity dynamics with the Diffused Vortex Hydrodynamics method

D. Durante [a], S. Marrone [a,*], D. Brömmel [b], R. Speck [b], A. Colagrossi [a]

[a] CNR-INM, Institute of Marine Engineering, Rome, Italy
[b] JSC, Jülich Supercomputing Centre, Forschungszentrum Jülich GmbH, 52425 Jülich, Germany

ARTICLE INFO

*Keywords:*
Vortex method
Particle methods
Meshless methods
Diffused Vortex Hydrodynamics
Vortex rings

ABSTRACT

In this paper the three-dimensional extension of the Diffused Vortex Hydrodynamics (DVH) is discussed along with free vorticity dynamics simulations. DVH is a vortex particle method developed *in-house* and widely validated in a 2D framework. The DVH approach has been embedded in a new frontend to the open-source code PEPC, the Pretty Efficient Parallel Coulomb solver. Within this parallel Barnes–Hut tree code, a superposition of elementary heat equation solutions in a cubic support is performed during the diffusion step. This redistribution avoids excessive clustering or rarefaction of the vortex particles, providing robustness and high accuracy of the method. An ascending vortex dipole at various resolutions is selected as a test-case and heuristic convergence measurements are performed, taking into account the conservation of prime integrals and the energy–enstrophy balance.

## 1. Introduction

In the Particle Vortex Methods (PVMs) the incompressible Navier–Stokes equations (NSEs) are solved in velocity–vorticity formulation. It follows that the fluid domain can be discretized by means of vortex particles which are present in the rotational region only. Therefore, the computational domain can be generally much smaller in comparison with other methods. Other relevant advantages of PVMs are: (i) the pressure field is not a direct unknown of the problem; (ii) the vortex particles are advected in the domain in a Lagrangian way, eliminating the numerical dissipation inherent to mesh-based approaches where the nonlinear convective terms of the NSEs need to be discretized; (iii) the boundary conditions at infinity are automatically satisfied, avoiding the need of large numerical domains (for more details see *e.g.* [13]).

In recent years, much of the interest on Lagrangian based approaches came from the growing interest in using parallel supercomputers or graphical processing units (GPUs) for large computations [41,52,60,61]. Moreover, the advent of Fast Mulitpole Methods (FMMs) optimized the computational costs and recent developments in numerical analysis allowed for the accurate treatment of viscous effects. As also remarked in [1], PVMs are nowadays an interesting strategic alternative to classic mesh-based methods (see *e.g.* [15,17,18,33,38]).

Historically, simulations with vortex methods date back to the thirties with hand calculations of the Kelvin–Helmholtz instabilities by Rosenhead [45,46]. For several decades the grid-free character and the physical attributes of vortex methods were exploited in the simulation of unsteady separated flows. Theoretical research on vortex methods provided a solid mathematical background for the evaluation of the accuracy and of the stability of the method [35,36].

* Corresponding author.
*E-mail address:* salvatore.marrone@cnr.it (S. Marrone).

https://doi.org/10.1016/j.matcom.2024.06.003
Received 15 February 2024; Received in revised form 14 May 2024; Accepted 4 June 2024
Available online 6 June 2024
0378-4754/© 2024 The Author(s). Published by Elsevier B.V. on behalf of International Association for Mathematics and Computers in Simulation (IMACS). This is an open access article under the CC BY-NC-ND license (http://creativecommons.org/licenses/by-nc-nd/4.0/).

Thanks to the pioneering works of Chorin [10,11], where the viscous splitting was introduced, the modern developments of vortex methods officially started (using random-walk methods for viscous effects) together with the three-dimensional calculations of Rehbach [43] and Leonard [36].

Motivated by the interest of applied mathematicians, first convergence analyses were carried out by Hald [29] and Beale and Majda [4]. Later Long [37] gave some convergence proofs of random-walk methods in two dimensions, while Hou [31] and Hou and Lowengrub [32] found convergence proofs for point vortex methods. In addition to these fundamental studies, many efforts have been devoted to overcoming the main intrinsic difficulties, related to the treatment of boundary conditions and the distortion of the particle distribution (see *e.g.* [34,53]).

A recent approach called Diffuse Vortex Hydrodynamics (DVH) is a vortex particle method in which the diffusion process is modeled by superposition of simple solutions of the heat equation [22,48–50]. For each vortex particle the diffusion is carried out over a circular area of radius $R_d$, called the "diffusive radius" which is a parameter of the simulation. The new particles correspond to points of a uniform lattice that regularize the spatial distribution of the vortices.

Successfully tested and validated in a 2D framework [15,17–19,51], a convergence analysis was discussed in [50], where the analytical solution of Lamb–Oseen vortex [42] was considered. The convergence of the method was tested for different Reynolds numbers and for several values of diffusive radius.

The use of particles leads to an $N-$body problem with intrinsic $\mathcal{O}(N^2)-$complexity. This can be overcome by using a fast multipole expansion [20], reducing the complexity to $\mathcal{O}(N \log N)$. In order to simplify this expansion, a class of algebraic kernels was introduced in [58]. Thanks to this approach, the three-dimensional parallel [3] open-source tree code PEPC, the *Pretty Efficient Parallel Coulomb solver* [25] was implemented. Based on the original Warren–Salmon 'hashed oct-tree' scheme [62] with a multipole expansion up to $p = 2$, it was initially developed by Gibbon [23] for mesh-free modeling of nonlinear, complex plasma systems [24,26]. It was later extended to become a general purpose framework for $\mathcal{O}(N \log N)$ tree code simulations through the development of *ad-hoc* frontends. It can perform complex simulations with up to $10^9$ particles routinely and has shown excellent scalability properties, *e.g.* with up to 294,912 cores on the IBM Blue Gene/P system JUGENE [65] and later with up to 1.8M threads on 458.752 cores of JUQUEEN [27], at the time both the largest systems at the Jülich Supercomputing Centre.

Adding to the previous vortex frontend [58], the PEPC-DVH frontend is a new development carried out in the last year and is aimed at implementing some DVH key features inside the PEPC tree code [16]. In this paper a convergence analysis of this new algorithm is discussed and compared to the classic two-dimensional DVH. In addition, the effect of some parameters, like the extension of the diffusive radius, are investigated.

The paper is organized as follows: in Section 2 the mathematical background behind the DVH splitting scheme is summarized with advection step detailed in Section 2.2 and the diffusion step in Section 2.3; the criterion of synchronization of advection/diffusion steps is indicated in Section 2.4; the conservation laws to be checked during numerical simulations are given in Section 3; finally, the numerical 2D and 3D simulations are discussed in Section 4. Conclusions are offered in Section 5.

## 2. Diffused vortex hydrodynamics

When the curl operator is applied to the Navier–Stokes momentum equation describing the flow field of a viscous fluid in a domain $\Omega$, the vorticity equation is obtained:

$$\frac{D\boldsymbol{\omega}}{Dt} = (\boldsymbol{\omega} \cdot \boldsymbol{\nabla})\, \boldsymbol{u} + \nu\, \nabla^2 \boldsymbol{\omega} \qquad \forall \boldsymbol{x} \in \Omega \tag{1}$$

where $\boldsymbol{\omega} \equiv \boldsymbol{\omega}(\boldsymbol{x}, t)$ represents the vorticity field and is a function of time and position, $\boldsymbol{u} \equiv \boldsymbol{u}(\boldsymbol{x}, t)$ the velocity field and $\nu$ the fluid kinematic viscosity. The first term on the right hand side describes the *stretching* or *tilting* of vorticity. This term represents one of the mechanisms with which the energy of large eddies is transferred to smaller scales. In 2D this term is zero and the inverse cascade moves energy away from small scales. The quantity $D\boldsymbol{\omega}/Dt$ represents the material derivative of the vorticity field and can be explicitly expressed as:

$$\frac{D\boldsymbol{\omega}}{Dt} = \frac{\partial \boldsymbol{\omega}}{\partial t} + (\boldsymbol{u} \cdot \boldsymbol{\nabla})\, \boldsymbol{\omega}$$

so the Eqs. (1) describe simultaneously both the advection and the diffusion of the vorticity field. The link between velocity and vorticity is given by the Poisson equation:

$$\nabla^2 \boldsymbol{u} = -\boldsymbol{\nabla} \times \boldsymbol{\omega}\ . \tag{2}$$

In order to solve it the velocity field can be decomposed according to the Helmholtz–Hodgetz decomposition theorem as [28]:

$$\boldsymbol{u} = \boldsymbol{u}_\omega + \boldsymbol{u}_\varphi$$

where the first term at right hand side is a rotational (divergence free) component, whereas the second one is a potential (curl free) component. The relation of these components with vorticity and potential fields is given by:

$$\boldsymbol{\omega} = \boldsymbol{\nabla} \times \boldsymbol{u}_\omega(\boldsymbol{x}, t) \qquad \boldsymbol{\nabla}\varphi = \boldsymbol{u}_\varphi(\boldsymbol{x}, t) + \boldsymbol{u}_\infty(t)$$

where the term $\boldsymbol{u}_\infty$ is related to the free-stream component.

In the present work, only free-vorticity test-cases are treated, hence, the term $\boldsymbol{u}_\varphi$ is neglected. We will refer generically to the velocity $\boldsymbol{u}$ meaning $\boldsymbol{u}_\omega$. Conversely, the component $\boldsymbol{u}_\varphi$ becomes crucial when the fluid domain is confined by boundaries and it is

used to enforced specific boundary conditions (see [22,34,48]). In unbounded space, the solution of the Poisson equation (2) is given by the Biot–Savart law as:

$$\boldsymbol{u}_\omega(\boldsymbol{x}) = \int_{\mathbb{R}^3} d\boldsymbol{y}\ \boldsymbol{K}(\boldsymbol{x}-\boldsymbol{y})\times\boldsymbol{\omega}(\boldsymbol{y}) = \boldsymbol{K}\circledast\boldsymbol{\omega}\,, \qquad \boldsymbol{K}(\boldsymbol{x}) = -\frac{\boldsymbol{x}}{4\pi|\boldsymbol{x}|^3}\,, \tag{3}$$

where $\boldsymbol{K}$ is called *Biot–Savart kernel* in 3D (for more details see *e.g.* [39,44]).

According to the well known operator splitting scheme [8,22,40] advection and diffusion steps can be considered separately during the computational procedure:

$$\begin{cases} \dfrac{D\boldsymbol{\omega}}{Dt} = (\boldsymbol{\omega}\cdot\boldsymbol{\nabla})\,\boldsymbol{u} \\ \dfrac{D\boldsymbol{x}}{Dt} = \boldsymbol{u} \end{cases} \quad + \quad \begin{cases} \dfrac{\partial\boldsymbol{\omega}}{\partial t} = \nu\nabla^2\boldsymbol{\omega} \\ \boldsymbol{u} = \boldsymbol{0} \end{cases}$$

The approximate solution of the governing equation is thus obtained by sequences of Eulerian (inviscid) steps and purely diffusive steps. The numerical solution scheme is based on a *viscous vortex method* originally discussed in [10,11], together with a deterministic diffusion algorithm [7].

### 2.1. Vorticity field discretization

As already clarified in [50], assuming the vorticity field as a measure, one can express it through the Lebesgue integral

$$\boldsymbol{\omega}(f) = \int f(\boldsymbol{x})\ \boldsymbol{\omega}\{d\boldsymbol{x}\} \tag{4}$$

where $f$ is a regular test function. By discretizing the vorticity field with $N$ point vortices, each one with vectorial circulation $\boldsymbol{\alpha}_i$ and position $\boldsymbol{x}_i$ one obtains:

$$\boldsymbol{\omega}(f) = \sum_{i=1}^{N}\int f(\boldsymbol{x})\,\boldsymbol{\alpha}_i\,\delta_{\mathbf{x}_i}\{d\mathbf{x}\} \qquad \text{with} \quad \int f(\mathbf{x})\ \delta_{\mathbf{x}_0}\{d\mathbf{x}\} = f(\mathbf{x}_0) \tag{5}$$

with $\delta_{\mathbf{x}_i}\{d\mathbf{x}\}$ the three-dimensional Dirac delta measure.

Rather than using a singular distribution, regularized smoothing kernels may be preferable in order to transform point particles into 'blobs' of finite core size.

**Definition 1.** A function $\zeta : \Omega\to\mathbb{R}$ for $\Omega=\mathbb{R}^d$, $d=2,3$ with $\zeta\in C^\infty(\Omega)$ is called *smoothing kernel* if it satisfies the *normalization constraint*:

$$\int_\Omega \zeta(y)\ dy = 1$$

**Definition 2.** A function $\zeta_\varepsilon : \Omega\to\mathbb{R}$ for $\Omega=\mathbb{R}^d$, $d=2,3$ with

$$\zeta_\varepsilon(x) = \frac{1}{\varepsilon^3}\ \zeta\left(\frac{x}{\varepsilon}\right)$$

is called *regularized smoothing kernel* with core size $\varepsilon>0$

**Definition 3.** A smoothing kernel $\zeta=\zeta^n$ is of order $n\in\mathbb{N}_0$ if the following *moment conditions* hold:

$$\int_\Omega \zeta(y)\ y^\beta\ dy = 0 \text{ for } 0<|\beta|<n-1 \text{ with multi-index } \beta$$
$$\int_\Omega |\zeta(y)|\ |y|^n\ dy < \infty\ .$$

Possible choices of the regularized smoothing function of order $n=2$ may be:

$$\zeta(\rho) = \frac{15}{8\pi}\ \frac{1}{(\rho^2+1)^{7/2}} \qquad \zeta(\rho) = \frac{3}{4\pi}\ \exp\left(-\rho^3\right)$$

where the left one is an algebraic kernel [5], while the right one is a Gaussian kernel [30].

As remarked in [58], it is crucial to limit the computational costs related to the evaluation of these kernels. Algebraic kernels are generally more convenient compared to Gaussian ones and, in this perspective, Speck [58] proposes a method for creating algebraic kernels of arbitrary order. This approach allows fast numerical calculations by discretizing the vorticity and the velocity fields as:

$$\boldsymbol{\omega}_\varepsilon(\boldsymbol{x},t) = \sum_{j=1}^{N}\boldsymbol{\alpha}_j(t)\ \zeta_\varepsilon(\boldsymbol{x}-\boldsymbol{x}_j) \qquad \boldsymbol{u}_\varepsilon(\boldsymbol{x},t) = \sum_{j=1}^{N}\boldsymbol{K}_\varepsilon(\boldsymbol{x}-\boldsymbol{x}_j)\times\boldsymbol{\alpha}_j(t) \tag{6}$$

where $N$ is the number of vortex particles and:

$$\boldsymbol{K}_\varepsilon(\boldsymbol{x}) = -\frac{\boldsymbol{x}}{|\boldsymbol{x}|^3}\int_0^{|\boldsymbol{x}|/\varepsilon} ds\ \zeta(s)\ s^2 \qquad \boldsymbol{\alpha}_j(t) = \int_{\mathcal{V}_j(t)} d\boldsymbol{x}\ \boldsymbol{\omega}(\boldsymbol{x},t)\sim\boldsymbol{\omega}(\boldsymbol{x}_j(t),t)\ \mathcal{V}_j(t) \tag{7}$$

where $\mathcal{V}_j(t)$ is the volume associated to the $j-$th vortex particle and centered on $\boldsymbol{x}_j(t)$ (see *e.g.* [13]). As remarked in [64], although the divergence of the velocity field $\boldsymbol{u}_\epsilon$ is null, this is not true for the divergence of $\boldsymbol{\omega}_\epsilon$:

$$\nabla \cdot \boldsymbol{\omega}_\epsilon = \sum_{j=1}^{N} \boldsymbol{\alpha}_j(t) \cdot \nabla(\zeta_\epsilon(\boldsymbol{x} - \boldsymbol{x}_j)) \neq 0$$

thus indicating that a superposition of non-solenoidal functions is used for representing a divergence-free field. Therefore, although $\boldsymbol{\omega}_\epsilon(\boldsymbol{x}, 0)$ is a good representation of $\boldsymbol{\omega}(\boldsymbol{x}, 0)$ at $t = 0$ (*i.e.* a divergence-free field is initialized), this is not necessarily true for $t > 0$. However, as it will be discussed later, the zero-divergence of the vorticity field can be recovered after the diffusion step.

From a computational point of view, the adoption of the vorticity as the primary variable avoids the discretization of the non-rotating regions, the computations being limited to the description of the vortical zones only.

### 2.2. Inviscid step

The inviscid evolution of the vortex particles is described by the Euler equation which requires the evaluation of the velocity field $\boldsymbol{u}(\boldsymbol{x}, t)$ at every time step. This evaluation is performed numerically through the formula (6) which require an amount of $\mathcal{O}(N^2)$ operations for the direct calculation of $\boldsymbol{u}$ at every vortex particle. A direct numerical implementation of this procedure is unfeasible in practice because it would require large computational costs, thus severely limiting the number of vortex particles handled by the algorithm. To overcome this issue, a multipole expansion approach [3] can be a convenient numerical strategy. This approach was implemented in the parallel tree code PEPC allowing to reduce to $\mathcal{O}(N \log N)$ the number of operations.

It is worth to underline that, although the convergence of the numerical method is not proved in the general viscous case, a theorem of convergence for the inviscid case can be demonstrated and it is recalled in Appendix.

Substituting the expressions (6) in the vorticity transport equation, the advection step can be rearranged [64] as:

$$\begin{cases} \dfrac{d\boldsymbol{x}_j}{dt} = \displaystyle\sum_{i=1}^{N} [\boldsymbol{K}_\epsilon(\boldsymbol{x}_j - \boldsymbol{x}_i) \times \boldsymbol{\alpha}_i] & \text{for } j = 1, \dots, N \\ \dfrac{d\boldsymbol{\alpha}_j}{dt} = -\displaystyle\sum_{i=1}^{N} \nabla \boldsymbol{K}_\epsilon(\boldsymbol{x}_j - \boldsymbol{x}_i) \cdot (\boldsymbol{\alpha}_j \times \boldsymbol{\alpha}_i) & \text{for } j = 1, \dots, N \end{cases} \tag{8}$$

where the first equation of system (8) defines the new vortex particles positions, whereas the second equation gives the corresponding circulation update. In the 2D version of the same algorithm, the right hand side of second equation of system (8) is null. System (8) is integrated in time by means of a 4th order Runge–Kutta scheme.

### 2.3. Diffusion

Viscous effects are accounted for in the diffusive step where the fluid velocity is neglected and the diffusion of the vorticity field is evaluated through the heat equation:

$$\frac{\partial \boldsymbol{\omega}}{\partial t} = \nu \nabla^2 \boldsymbol{\omega} \tag{9}$$

where, differently from the advection step, $\boldsymbol{\omega}$ is here represented as a superposition of exact solutions [6,7]:

$$\boldsymbol{\omega}(\boldsymbol{x}, t) = \frac{\boldsymbol{\alpha}_0}{\sqrt{(4\pi\nu\Delta t)^3}} \exp\left(-\frac{|\mathbf{x} - \mathbf{x}_0|^2}{4\nu\Delta t}\right) \tag{10}$$

related to a single point vortex at time $t_0$ with initial circulation $\boldsymbol{\alpha}_0$ and position $\boldsymbol{x}_0$ as initial datum. As remarked in [50], in two dimensions the solution is the well known Lamb–Oseen vortex.

Similarly to Rossi et al. [49], through the diffusion the vorticity is redistributed on a Cartesian lattice, whose points become the new set of vortex particles. Indeed, as clarified in *e.g.* [2,21], the Lagrangian vortex methods suffer of excessive clustering or rarefaction of the vortex particles and a redistribution procedure is often needed to mitigate the problem. By means of the adopted diffusion procedure this requirement is automatically fulfilled because a disordered set of vortex particles is replaced by an ordered set at the end of the diffusive step.

Starting with all the circulation concentrated at time $t_0$ on a single point vortex, for $t_0 + \Delta t$ the distribution of vorticity should cover all $\mathbb{R}^3$. This would result in a computationally impractical situation. Therefore, a radius $R_d$, called *diffusive radius*, is defined to make the support of (10) compact. According to this definition, it results:

$$\begin{cases} \boldsymbol{\omega}(\boldsymbol{x}, t_0 + \Delta t) = \dfrac{\boldsymbol{\alpha}_0}{\sqrt{(4\pi\nu\Delta t)^3}} \exp\left(-\dfrac{|\mathbf{x} - \mathbf{x}_0|^2}{4\nu\Delta t}\right) & \text{if} \quad |\mathbf{x} - \mathbf{x}_0| \leq R_d \\ \boldsymbol{\omega}(\mathbf{x}, t_0 + \Delta t) = \mathbf{0} & \text{otherwise} \end{cases} \tag{11}$$

where $R_d$ is the radius of the truncated support. Similarly to what was remarked in [50] for a 2D approach, an error $\xi$ in the conservation of the circulation is inevitably introduced:

$$\xi = \left| \frac{\boldsymbol{\alpha}(t_0 + \Delta t) - \boldsymbol{\alpha}_0}{\boldsymbol{\alpha}_0} \right| \tag{12}$$

where $\boldsymbol{\alpha}(t_0 + \Delta t)$ is the circulation enclosed at time $t_0 + \Delta t$ in a sphere of radius $R_d$. A simple integration of (10) gives for $\boldsymbol{\alpha}(t)$ the following expression:

$$\boldsymbol{\alpha}(t) = \boldsymbol{\alpha}_0 \left[ \operatorname{erf}\left( \frac{R_d}{\sqrt{4\nu\Delta t}} \right) - \frac{2R_d}{\sqrt{4\pi\nu\Delta t}} \exp\left( -\frac{R_d^2}{4\nu\Delta t} \right) \right] \tag{13}$$

and by substituting this relation into (12) one obtains:

$$\xi = \operatorname{erfc}\left( \frac{1}{\sqrt{\beta}} \right) + \frac{2}{\sqrt{\pi\beta}} \exp\left( -\frac{1}{\beta} \right) \qquad \text{with} \qquad \beta = \frac{4\nu\Delta t}{R_d^2} \tag{14}$$

which is a non-linear equation in $\beta$.

Similarly to what has been done in [48] for the 2D framework, we consider a trade-off between accuracy and computational speed by accepting an error on $\xi = 10^{-5}$. Thus, by developing the expression (14) in Taylor series an approximate value for $\beta$ is obtained:

$$\beta = \frac{4\nu\Delta t}{R_d^2} \approx 0.077 \tag{15}$$

which links the diffusive radius and the time step $\Delta t$.

As remarked in [48], diffusive and advective time steps are generally different so that it is preferable to distinguish them as $\Delta t_d$ and $\Delta t_a$. Using the expression (15), the following relations hold:

$$\Delta t_d \frac{U}{L} = \left( \frac{R_d/\Delta x}{L/\Delta x} \right)^2 \left( \frac{\beta}{4} \right) \mathrm{Re} \tag{16}$$

where $U$ and $L$ are the reference velocity and the reference length, respectively. The quantity $\Delta x$ is the spatial resolution of the Cartesian lattice, while Re is the Reynolds number $\mathrm{Re} = UL/\nu$.

The relation (16) allows for the evaluation of the diffusive time step from:

- the adopted spatial resolution $L/\Delta x$
- the diffusive radius $R_d$
- the Reynolds number

once the error $\xi$ has been fixed (as mentioned above, $\xi = 10^{-5}$ is considered here).

As stated above, the vorticity field is lumped into point vortices located at the nodes of the lattice after the diffusion. However, the use of a Cartesian lattice with a uniform spacing is not a real constraint for the DVH model, and the procedure can be generalized on non uniform meshes (see *e.g.* [48]).

Call $\boldsymbol{x}_i$ the position of a generic node $i$ of the lattice within a distance $R_d$ from a vortex $j$ in position $\boldsymbol{y}_j$ with circulation $\boldsymbol{\alpha}_j$. During the diffusive time step $\Delta t_d$, the vortex $j$ gives a contribution $\boldsymbol{\alpha}_{ij}$ to the circulation of $i$ equal to:

$$\boldsymbol{\alpha}_{ij} = \frac{\boldsymbol{\alpha}_j}{\sqrt{(4\pi\nu\Delta t)^3}} \exp\left( -\frac{|\boldsymbol{x}_i - \boldsymbol{y}_j|^2}{4\nu\Delta t} \right) \Delta x^3 = \boldsymbol{\alpha}_j \, w_{ij} \, \Delta x^3 \tag{17}$$

where the expression (10) has been used and $w_{ij}$ is a bell-shaped function depending on the distance between $\boldsymbol{x}_i$ and $\boldsymbol{y}_j$. In order to enforce the conservation of the circulation of each vortex, the contribution $\boldsymbol{\alpha}_{ij}$ is renormalized through a Shepard procedure [57]:

$$\boldsymbol{\alpha}'_{ij} = \boldsymbol{\alpha}_j \frac{w_{ij}}{\sum_{i \in \mathcal{P}_j} w_{ij}} \tag{18}$$

where $\mathcal{P}_j$ is the set of lattice points falling in the sphere of radius $R_d$ centered on $\boldsymbol{y}_j$ (see Fig. 1 for a sketch). Finally, the circulation of the new vortex at node $\boldsymbol{x}_i$ is expressed as:

$$\boldsymbol{\alpha}_i = \sum_{j \in \mathcal{B}_i} \boldsymbol{\alpha}'_{ij} \tag{19}$$

where $\mathcal{B}_i$ is the set of vortices falling in the sphere of radius $R_d$ centered on $\boldsymbol{x}_i$. In order to limit the number of vortices generated during the diffusive process, the new particles with vorticity $\boldsymbol{\alpha}_i/\mathcal{V}_i$ with module lower than a fixed cut-off, $\omega_{cut}$, are removed, similarly to Winckelmans and Leonard [64], Speck [58] and Rossi et al. [50].

### 2.4. Choice of the time steps

As outlined in Section 2.3, the advection and the diffusion of the point vortices are considered separately, so that two different time steps are taken into account: for advection $\Delta t_a$ and for diffusion $\Delta t_d$. From formula (16) it is clear that the diffusion time step $\Delta t_d$ depends on Re and on the diffusive radius $R_d$. The number of points inside the radius $R_d$ for a lattice characterized by a uniform spacing $\Delta x$ is:

$$N_{node} = \left\lfloor \frac{4}{3}\pi \left( \frac{R_d}{\Delta x} \right)^3 \right\rfloor \tag{20}$$

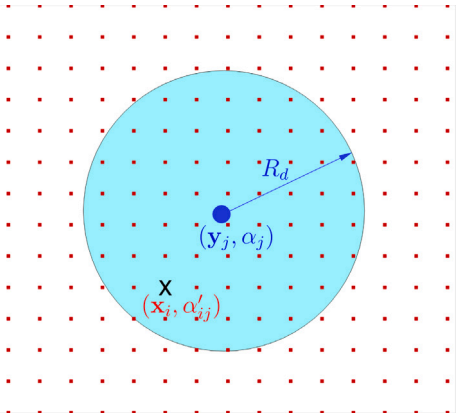


**Fig. 1.** Sketch of the vorticity diffusion of a vortex particle $j$ onto a Cartesian lattice. The set of lattice points $P_j$ falling inside the sphere of radius $R_d$, centered on the particle $\boldsymbol{y}_j$, receive a circulation contribution $\boldsymbol{\alpha}'_{ij}$ from particle $j$.

being $\lfloor x \rfloor$ the largest integer not greater than $x$.

It is important to underline that $N_{node}$ (or equivalently the ratio $R_d/\Delta x$) together with $\Delta x$ are the key parameters of the DVH model, because they fix the discretization level used in the particle method. A typical number for $N_{node}$ in 3D is 270 which corresponds to a ratio $R_d/\Delta x$ equal to 4.

Conversely, the advection step $\Delta t_a$ is determined once the flow velocity $U$ and the discretization $\Delta x$ used during the diffusion step are fixed. The time interval between two diffusive time steps should be short enough to avoid that the vortex particle distribution becoming too irregular. The advection time step can be straightforwardly defined as:

$$\Delta t_a = \mathrm{Co}\,\frac{\Delta x}{U} \;\Rightarrow\; \Delta t_a \frac{U}{L} = \mathrm{Co}\,\frac{1}{(L/\Delta x)} \tag{21}$$

where Co is the Courant number. As remarked in [13,50], the stability constraints on the Co number, typical of other numerical methods, are less restrictive for vortex method schemes based on operator splitting, as the present DVH, even allowing Co $> 1$. However, as underlined in [12], Co should never be too large to avoid a displacement of particles larger than the size of the particles, which would lead to particle configurations that are too disordered.

Once $\Delta t_a$ is evaluated, it needs to be rearranged for synchronizing diffusion and advection, therefore, $\Delta t_d$ and $\Delta t_a$ need to be in integer ratio, *i.e.*

$$N_{\Delta t} = \left\lceil \frac{\Delta t_d}{\Delta t_a} \right\rceil \qquad \Rightarrow \qquad \Delta t_a^{new} = \frac{\Delta t_d}{N_{\Delta t}} \tag{22}$$

being $\lceil x \rceil$ the lowest integer greater than $x$. From the above expression it is clear that when $N_{\Delta t} = 1$, the time steps $\Delta t_a$ and $\Delta t_d$ are the same and a diffusive step is performed every advective step (this is a typical condition when simulating low Reynolds numbers flow where $\Delta t_d$ becomes similar or even smaller than $\Delta t_a$).

Using the constraints on time-steps, the Eqs. (16), (21) and (22) can be rearranged and a relation between the $N_{\Delta t}$, the spatial resolution $L/\Delta x$ and the Reynolds number can be obtained:

$$N_{\Delta t} = \left\lceil \frac{\beta}{4} \frac{(R_d/\Delta x)^2}{\mathrm{Co}} \right\rceil \mathrm{Re}_{\Delta x}\,, \qquad \mathrm{Re}_{\Delta x} = \frac{\mathrm{Re}}{L/\Delta x} \tag{23}$$

where $\mathrm{Re}_{\Delta x}$ is the so called Reynolds-cell number. By setting the ratio $R_d/\Delta x$ to a typical value of 4, $\beta = 0.077$ and Co $= 1$, the term in brackets is $\simeq 3$ (both in 2D and in 3D frameworks). Following the analysis performed in [50], in order to have an accurate solution, the Reynolds-cell should be of order of one. From Eq. (23) it follows that when the value of $N_{\Delta t}$ is smaller than 3 the $\mathrm{Re}_{\Delta x}$ is in the right range for studying properly the vortex dynamics. Furthermore, in [50] the authors show that when $N_{\Delta t}$ is lower than 10, the asymptotic range of convergence is always obtained.

## 3. Conservation laws

### 3.1. Continuous formulation

For three-dimensional unbounded inviscid flows, there are three linear invariants associated to the conservation of total vorticity, linear and angular impulse [64]:

$$\boldsymbol{\Omega} = \int_{\mathbb{R}^3} d\boldsymbol{x}\; \boldsymbol{\omega} = \mathbf{0} \tag{24}$$

$$\boldsymbol{I} = \int_{\mathbb{R}^3} d\boldsymbol{x}\ \boldsymbol{u} = \frac{1}{2}\int_{\mathbb{R}^3} d\boldsymbol{x}\ \boldsymbol{x}\times\boldsymbol{\omega} \tag{25}$$

$$\boldsymbol{A} = \int_{\mathbb{R}^3} d\boldsymbol{x}\ \boldsymbol{x}\times\boldsymbol{u} = \frac{1}{3}\int_{\mathbb{R}^3} d\boldsymbol{x}\ \boldsymbol{x}\times(\boldsymbol{x}\times\boldsymbol{\omega}) \tag{26}$$

that are conserved also for viscous flows. Using the Helmholtz decomposition introduced in Section 2, the velocity field is described as:

$$\boldsymbol{u} = \boldsymbol{\nabla}\times\boldsymbol{\psi}$$

where $\boldsymbol{\psi}$ is the 3D stream function. The kinetic energy is thus expressed as:

$$\begin{aligned} E_k &= \frac{1}{2}\int_{\mathbb{R}^3} d\boldsymbol{x}\ \boldsymbol{u}\cdot\boldsymbol{u} = \frac{1}{2}\int_{\mathbb{R}^3} d\boldsymbol{x}\ (\boldsymbol{\nabla}\times\boldsymbol{\psi})\cdot(\boldsymbol{\nabla}\times\boldsymbol{\psi}) \\ &= \frac{1}{2}\int_{\mathbb{R}^3} d\boldsymbol{x}\ \boldsymbol{\psi}\cdot[-\nabla^2\boldsymbol{\psi} + \boldsymbol{\nabla}(\boldsymbol{\nabla}\cdot\boldsymbol{\psi})] \\ &= \frac{1}{2}\int_{\mathbb{R}^3} d\boldsymbol{x}\ \boldsymbol{\psi}\cdot\boldsymbol{\omega} + \cancel{\frac{1}{2}\int_{\mathbb{R}^3} d\boldsymbol{x}\ \boldsymbol{\psi}\cdot\boldsymbol{\nabla}(\boldsymbol{\nabla}\cdot\boldsymbol{\psi})} \end{aligned} \tag{27}$$

where the second term at right hand side is theoretically zero because $\boldsymbol{\psi}$ is a solenoidal field. However, this is not true when the description (6) is adopted, although it remains negligible as long as $\boldsymbol{\omega}$ remains a good representation of the vorticity field. In the viscous case the time derivative of the kinetic energy is related to the enstrophy [55]:

$$\frac{dE_k}{dt} = -\nu\int_{\mathbb{R}^3} d\boldsymbol{x}\ \boldsymbol{\omega}\cdot\boldsymbol{\omega} = -\nu\ \mathscr{E} \tag{28}$$

where $\mathscr{E}$ is the enstrophy function.

### 3.2. Discrete formulation

When a discrete description of the vorticity field is adopted, the relations (24)–(26) change accordingly:

$$\boldsymbol{\Omega} = \sum_{i=1}^{N}\boldsymbol{\alpha}_i(t) \qquad \boldsymbol{I} = \frac{1}{2}\sum_{i=1}^{N}\boldsymbol{x}_i(t)\times\boldsymbol{\alpha}_i(t) \qquad \boldsymbol{A} = \frac{1}{3}\sum_{i=1}^{N}\boldsymbol{x}_i(t)\times[\boldsymbol{x}_i(t)\times\boldsymbol{\alpha}_i(t)]\ . \tag{29}$$

The conservation of the total circulation is derived, considering the expression of $d\boldsymbol{\omega}/dt$ during the advective step, as follows:

$$\frac{d\boldsymbol{\Omega}}{dt} = -\sum_{i,j=1}^{N}\boldsymbol{\nabla}\boldsymbol{K}_{ij}\cdot(\boldsymbol{\alpha}_i\times\boldsymbol{\alpha}_j) = 0 \tag{30}$$

being $\boldsymbol{K}_{ij} = \boldsymbol{K}(\boldsymbol{x}-\boldsymbol{x}_j)|_{\boldsymbol{x}=\boldsymbol{x}_i}$ and considering that $\boldsymbol{\nabla}\boldsymbol{K}_{ij} = \boldsymbol{\nabla}\boldsymbol{K}_{ji}$ (see [64]). For the linear impulse, the conservation is obtained from the time derivative as:

$$\frac{d\boldsymbol{I}}{dt} = -\sum_{i,j=1}^{N}\boldsymbol{\alpha}_i\times(\boldsymbol{K}_{ij}\times\boldsymbol{\alpha}_j) \tag{31}$$

which is small as long as $\boldsymbol{\omega}$ remains a good representation of the vorticity field. The conservation of the angular impulse is typically not considered in its discrete form in literature, because it is hard to rearrange. However, a possible short expression could be the following one:

$$\frac{d\boldsymbol{A}}{dt} = \frac{1}{3}\sum_{i=1}^{N}\frac{d}{dt}[\boldsymbol{x}_i\times(\boldsymbol{x}_i\times\boldsymbol{\alpha}_i)] = \frac{1}{3}\sum_{i=1}^{N}[\boldsymbol{u}_i\times(\boldsymbol{x}_i\times\boldsymbol{\alpha}_i) - \boldsymbol{x}_i\times(\boldsymbol{\alpha}_i\times\boldsymbol{u}_i)] \tag{32}$$

where $\boldsymbol{u}_i = \sum_j \boldsymbol{K}_{ij}\times\boldsymbol{\alpha}_j$ and the derivative of cross product between $\boldsymbol{x}_i$ and $\boldsymbol{\alpha}_i$ is rearranged according Winckelmans and Leonard [64]. Similarly, the kinetic energy and the enstrophy have their discrete definitions as:

$$E_k = \frac{1}{8\pi}\sum_{\substack{i,j=1\\ i\neq j}}^{N}\frac{\boldsymbol{\alpha}_i\cdot\boldsymbol{\alpha}_j}{|\boldsymbol{x}_i-\boldsymbol{x}_j|} \tag{33}$$

$$\mathscr{E} = \sum_{i,j=1}^{N}\boldsymbol{\alpha}_i\cdot\boldsymbol{\alpha}_j\int_{\mathbb{R}^3} d\boldsymbol{x}\ \delta(\boldsymbol{x}-\boldsymbol{x}_i)\ \delta(\boldsymbol{x}-\boldsymbol{x}_j) = \sum_{i,j=1}^{N}\boldsymbol{\alpha}_i\cdot\boldsymbol{\alpha}_j\ \delta(\boldsymbol{x}_i-\boldsymbol{x}_j) = \sum_{i=1}^{N}|\boldsymbol{\alpha}_i|^2 \tag{34}$$

and the energy–enstrophy relation is obtained integrating in time Eq. (28):

$$\frac{1}{8\pi}\sum_{\substack{i,j=1\\ i\neq j}}^{N}\frac{\boldsymbol{\alpha}_i(t)\cdot\boldsymbol{\alpha}_j(t)}{|\boldsymbol{x}_i(t)-\boldsymbol{x}_j(t)|} - E_k(t_0) + \nu\sum_{i=1}^{N}\int_{t_0}^{t} dt'\ |\boldsymbol{\alpha}_i|^2(t') = 0 \tag{35}$$

where $E_k(t_0)$ is the initial kinetic energy of the particle system. It is worth clarifying that the last addendum of Eq. (35) is zero during the advection step (see Section 2) and it varies only during the diffusion step. In the following, the conservation Eqs. (30)–(32) are checked during time evolution, together with the energy–enstrophy relation (35). These equations are evaluated at different resolutions for the evolution of a single vortex ring.

It must be emphasized that, the final order of convergence of the overall numerical scheme is hard to assess theoretically because many error sources combine in the final solution: *i.* the approximation of the Poisson equation (2) which depends on the spatial resolution $\Delta x$ and the approximation linked to the FMM (see *e.g.* [47,58]); *ii.* the error related to the vorticity diffusion (9) which depends on the $R_d/\Delta x$ ratio and on the $\xi$ parameter (12); *iii.* the error in the time integration of the particle advection and diffusion. Moreover, the combination of these error sources are problem dependent as stressed in *e.g.* [50]. As a consequence, the convergence of the scheme is proven only empirically in Section 4.2 on a well established benchmark test-case.

## 4. Numerical validation

### 4.1. Single vortex ring evolution

As remarked in [63], the behavior of vortex rings has been studied intensively and it is a good test case for checking the capability of a numerical method Shankar and Dommelen [56]. The evolution of a vortex ring at intermediate Reynolds number is a case initially discussed in [59], where it reproduces an old experiment of Didden [14]. During the experiments, vortex rings were generated by impulsively forcing a column of fluid through a nozzle. The ring forms from the rolling-up of the vortex sheets created by the boundary layer along the walls of the nozzle.

After an initial transient, the ring evolution is essentially driven by $\Gamma/\nu$ and $a/R$ where $\Gamma$ is the circulation associated to the ring (*i.e.*, the circulation of the ring section), $R$ the radius of the ring and $a$ the radius of the section of the ring, also known as the *core* of the ring. In the core of the ring, where $a < R$, the solution is locally two-dimensional and the streamlines are nearly circular. With this assumptions the tangential velocity distribution is:

$$u_\tau = \frac{\Gamma}{2\pi s}\left[1 - \exp\left(-\frac{s^2}{4\nu t}\right)\right]$$

where $s$ is the distance from the core center. The quantity $a$ is defined as the distance of maximum value of $u_\tau$ from the core center, so that it can be found by solving $du_\tau/ds = 0$. The solution of the equation gives $a = 2\sqrt{K\nu t}$, so the ring core radius increase with time because of the viscosity effect (the constant $K = 1.25644$). The distribution of vorticity over the core is given by classic Gaussian Oseen solution [42] and it becomes in this case:

$$\omega = \frac{K}{\pi}\frac{\Gamma}{a^2}\exp\left[-K\left(\frac{R^2+r^2}{a^2} - \frac{2Rr}{a^2}\cos\theta\right)\right] \tag{36}$$

where $r$ is the distance of a point of the ring $\boldsymbol{x}$ from the ring center $\boldsymbol{x}_0$ (which coincides with the axes origin) and $s = \sqrt{R^2 + r^2 - 2Rr\cos\theta}$, $\theta$ being the angle between the vector $\boldsymbol{x} - \boldsymbol{x}_0$ and the horizontal plane (z = 0 plane in Fig. 2). Initially, $\Gamma = 1$, $R = 1$, the core radius is $c = 0.5R$ and $a/R = 0.35$ with $Re_\Gamma = \Gamma/\nu = 500$. The number of points along the core radius $N = R/\Delta x$ will be the parameter used for indicating the spatial resolution adopted.

### 4.2. Numerical results

In order to perform a correct investigation of the convergence properties of the DVH scheme in the standard benchmark of 3D vortex ring evolution, the 2D simplified problem is investigated at first. The effect of the diffusive radius, one of the most important parameters used for the simulation, is considered at varying resolution. The 2D restriction allows the adoption of resolutions up to $N = 128$, which are rather demanding in a 3D framework. As initial condition in 2D, two circular vorticity distributions (with centers $2R$ apart) are considered, corresponding to the transversal section of the ring, sketched in the top frame of Fig. 2.

The left frame resembles the condition indicated in literature [59,63] with the vortices initially distributed along concentric circles. After a series of numerical tests we found that the diffusion of these vortices on a Cartesian lattice induces a significant error after the first diffusion step, in particular on the energy–enstrophy Eq. (35). For this reason, we prefer to use an initial distribution on the points of a Cartesian lattice, as sketched in the top-right frame of Fig. 2. The same Cartesian distribution is used for 2D simulations as well.

As discussed in [59] and in [63] the dynamics of the ring is a simple rising movement along the central axis with diffusion, summarized in the bottom frame of Fig. 2. The most evident effect of the diffusion is the widening of the inner core, as expected from theory (see Section 4.1) and shown in Fig. 3 in 2D framework. Due to the fact that in 2D we are actually simulating two disconnected circular vortex patches, the characteristic time of the rising motion is significantly different between 2D and 3D. At $t\Gamma/R^2 = 50$ the 3D ring is at about the same height of the 2D solution at time $t\Gamma/R^2 = 100$ so that a factor of about 2 on the evolution time is found.

By considering that the rising time of the vortex ring depends on the value of the initial impulse component along the rising direction (the other two are constantly null) $I_0$, which is:

$$I_0^{3D} = \pi\int_0^\pi d\theta\int_0^\infty dr\ \omega\ r\ (r\sin\theta)^2 \qquad \text{and} \qquad I_0^{2D} = 2\int_{-\pi}^\pi d\theta\int_0^\infty dr\ \omega\ r^2\sin\theta$$

according to Stanaway [59] and Saffman [55]. It is worth to note that $I_0^{3D}$ and $I_0^{2D}$ are not dimensionally homogeneous, indeed, it is found that a non-dimensional estimation is:

$$\frac{I_0^{3D}}{\Gamma R^2} \approx 3.295 \qquad \text{and} \qquad \frac{I_0^{2D}}{\Gamma R} \approx 2 \qquad \Rightarrow \qquad I_0^{3D} \approx 1.65\ I_0^{2D}\ R$$

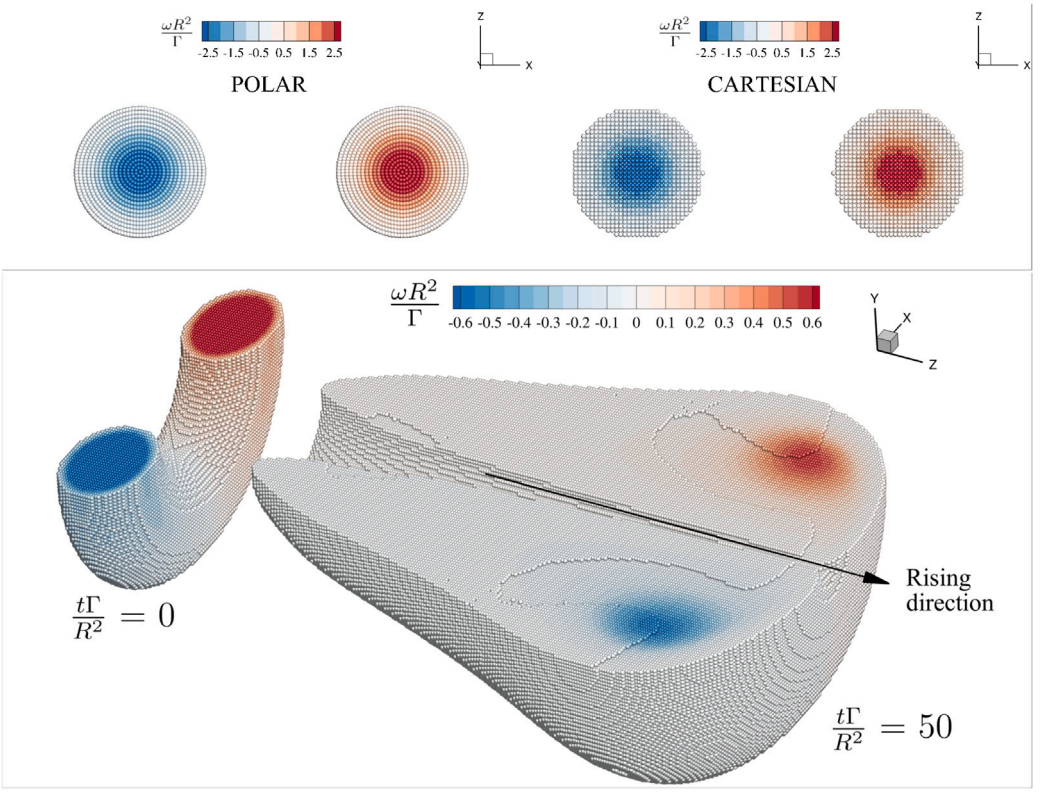


**Fig. 2.** **Top**: vortex ring vorticity distribution over the ring core at $N = 32$ (contour map is indicated at the top) as in [63] (**left**) and on Cartesian grid (**right**). **Bottom**: 3D vortex ring configurations (and $y$–vorticity distribution) at $t\Gamma/R^2 = 0$ and $t\Gamma/R^2 = 50$. Only particles with vorticity module $|\omega R^2/\Gamma| > 10^{-2}$ are shown.

being $\Gamma = 1$ and $R = 1$, the 3D ring possesses a larger initial impulse than the 2D dipole and, for this reason, moves faster. The time shift between 3D and 2D solutions is harder to estimate theoretically. In fact, if one considers the velocity of the ring centroid, as defined in [55], it depends on the linear impulse and on the time distribution of the vortex particles . Moreover, the same definition is not directly applicable in 2D [54]. As shown in [59], this velocity varies with time, making a direct determination of the time shift between 3D and 2D solution not trivial and out of the scope of the present work.

The convergence of the 2D solutions for kinetic energy and enstrophy in $L^2$ norm is shown in the top frame of Fig. 4 for different $R_d$. For the present study, four resolutions are considered: $N = 8$, $N = 16$, $N = 32$ and $N = 128$. The reported quantities are calculated as:

$$\mathrm{Err}_{E_k}^{N+1} = \left[\frac{1}{T}\int_{t_0}^{T} dt \;\left|E_k^N(t) - E_k^{N+1}(t)\right|^2\right]^{1/2} \Big/ \left[\frac{1}{T}\int_{t_0}^{T} dt \; E_k^{N_{max}}(t)\right] \tag{37}$$

where $t_0$ and $T$ are the initial and final simulation times, respectively, and $N_{max}$ refers to the maximum resolution used for the simulations. The same estimation is used also for $\mathcal{E}$. The convergence is shown for $R_d/\Delta x = 3, 4, 5, 6$, while the case $R_d/\Delta x = 2$ is dumped. Energy and enstrophy are not convergent in the latter case and the inclusion of the corresponding errors would make the plots difficult to read. As indicated below, we show the cases $R_d/\Delta x = 2$ only on Energy–Enstrophy balance, where the divergence of the solution can be appreciated.

The use of different points for the diffusive radius has no particular influence on the kinetic energy convergence, whereas $R_d/\Delta x = 3$ does not lead to a good convergence rate for enstrophy (see top-right frame of Fig. 4). Adopting $R_d/\Delta x = 4, 5$ seems almost indifferent with respect to convergence properties, so that $R_d/\Delta x = 4$ appears a good compromise between computational costs and accuracy. Moreover, the slope corresponding to order 2 convergence is reported in both top frames of Fig. 4. The numerical method exhibits a 2nd order convergence rate for both energy and enstrophy.

The energy–enstrophy relation (28) can be evaluated directly for every resolution and its convergence is analyzed through the quantity:

$$\mathrm{Err}_{E_k|\mathcal{E}}^{N} = \left[\frac{1}{T}\int_{t_0}^{T} dt \;\left(E_k^N(t) - E_k^N(t_0) + \nu\int_{t_0}^{t} dt' \mathcal{E}^N(t')\right)^2\right]^{1/2} \Big/ \left[\frac{1}{T}\int_{t_0}^{T} dt \; E_k^{N_{max}}(t)\right] \tag{38}$$

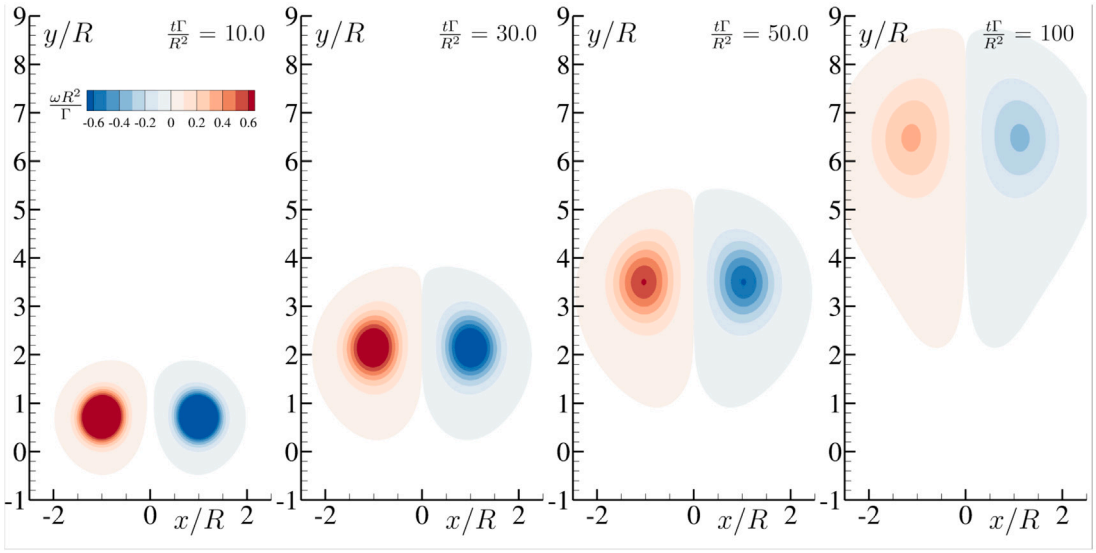


**Fig. 3.** 2D vortex ring evolution at $N = 256$ (contour map is indicated at the top of leftmost frame) and $R_d = 4$. Ratio between diffusive and advective time steps is $N_{\Delta t} = 1$. Only particles with vorticity module $|\omega R^2/\Gamma| > 10^{-3}$ are shown.

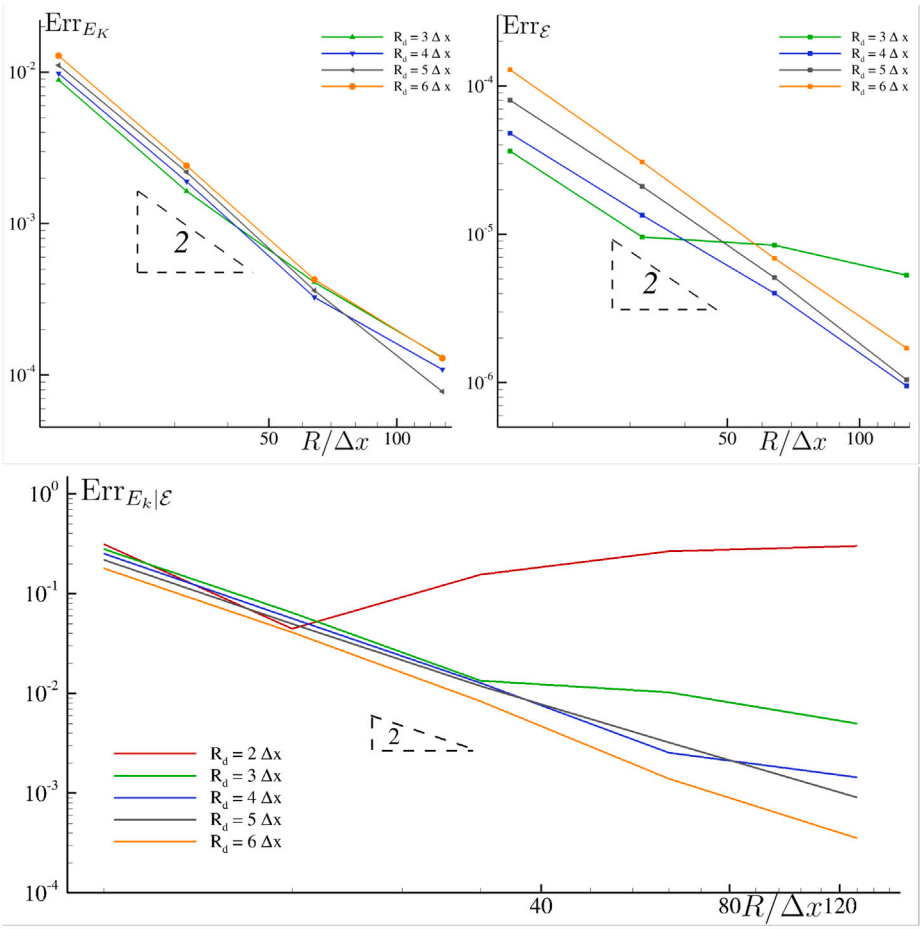


**Fig. 4. Top**: convergence of the $L^2$ norm between two subsequent resolutions for Energy (**left**) and Enstrophy (**right**) in 2D simulations for different values of $R_d$ and for resolutions up to $N = 128$. **Bottom**: convergence of energy–enstrophy conservation according to formula (38) for different values of $R_d$ and for resolutions up to $N = 128$. Second order slope is also reported.

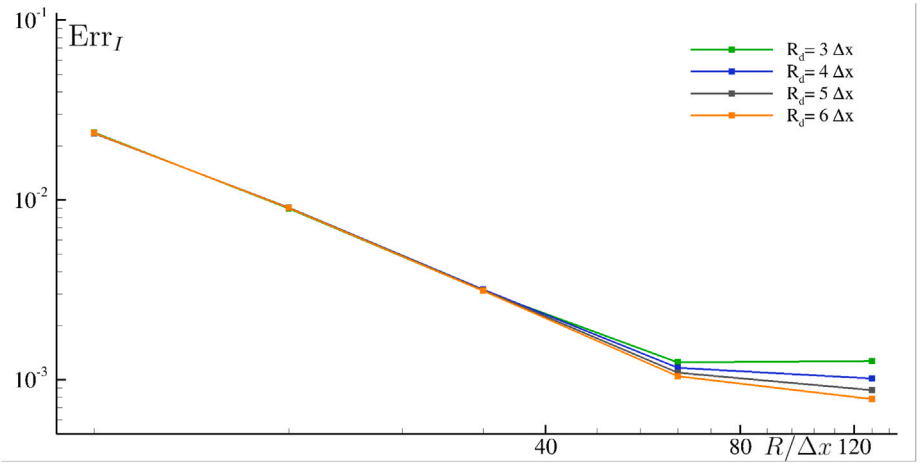


**Fig. 5.** Convergence of the linear impulse error $\mathrm{Err}_I$ in 2D simulations for different values of $R_d$ and for resolutions up to $N = 128$.

The convergence of quantity (38) is depicted in the bottom frame of Fig. 4 for $R_d/\Delta x = 2, 3, 4, 5, 6$. As expected, the less points are used in the diffusive radius, the larger is the error $\mathrm{Err}_{E_k|\mathcal{E}}$; in the limit case $R_d/\Delta x = 2$ a divergent behavior is observed. Also in this case, the scheme works very similarly for $R_d/\Delta x = 4, 5$. Similarly to $E_k$ and $\mathcal{E}$, also in this case a 2nd order convergence is observed.

Regarding the conserved quantities, we observe that the angular impulse $\boldsymbol{A}$ is identically null in 2D with open boundary conditions, because of the asymptotic exponential decay of $\omega$. Also, the total vorticity is conserved at machine precision ($10^{-12}$) in 2D simulations, while the error on linear impulse is shown in Fig. 5. The impulse should be constant during the simulation, so the error at resolution $N$ is calculated as:

$$\mathrm{Err}_I^N = \frac{1}{T}\int_{t_0}^{T} dt\ \frac{|\boldsymbol{I}^N(t) - \boldsymbol{I}_0^{ana}|}{|\boldsymbol{I}_0^{ana}|}$$

where $\boldsymbol{I}_0^{ana}$ is the analytical estimation of the linear impulse (constant in time).

A convergence trend is observed for $R_d/\Delta x = 3, 4, 5, 6$ and for the highest resolution the influence of the diffusive radius becomes evident. Again, similarly to Fig. 4, the larger the ratio $R_d/\Delta x$, the smaller the error.

The corresponding convergence analysis performed in 2D and summarized in Fig. 4 is carried out in 3D and shown in Fig. 6. In 3D, we limit our investigation to $N = 8$, 16, 32, 64 ($N = 128$ being too demanding in terms of computational resources), and to diffusive radii $R_d/\Delta x = 3$, 4, 5. Similarly to the 2D case, for the lowest $R_d/\Delta x$ ratio a non-convergent behavior is observed. This applies in particular for the kinetic energy, whereas for the enstrophy a convergence is observed for all values of $R_d/\Delta x$. The rate of convergence is close to order 2 for both $E_k$ and $\mathcal{E}$ at $R_d/\Delta x = 4, 5$. In the bottom frame of Fig. 6, the error on the energy–enstrophy relation (38) is shown for the same resolution and at varying diffusive radius. Both $R_d/\Delta x = 4, 5$ show good convergence rates as in 2D. Although $R_d/\Delta x = 5$ appears slightly better in terms of convergence properties, the choice $R_d/\Delta x = 4$, already selected as the best compromise in 2D, confirms to be valid also in 3D.

Differently from the 2D case, the total circulation $\boldsymbol{\Omega}$ in 3D is not exactly preserved for every resolution but a convergence rate is observed in the left frame of Fig. 7 for different diffusive radii. The condition $R_d = 4\Delta x$ is the only one that manifests a strictly monotonic convergence, whereas the condition $R_d = 3\Delta x$ does not exhibits a convergence when passing from $N = 16$ to $N = 32$. Similarly, also for the linear impulse (middle frame of Fig. 7) the choice $R_d/\Delta x = 3$ does not show a clear convergence, whereas it is attained for $R_d/\Delta x = 4, 5$. Finally, the right frame of Fig. 7 shows the convergence of the angular impulse $\boldsymbol{A}$. This quantity is not generally conserved by vortex methods: as stated in [64] it is conserved as long as $\omega_\varepsilon$ is a good representation of a divergence-free field. For all the investigated diffusive radii, the conservation seems attained and convergent, although not monotonically.

In general, we can conclude, from the present investigation that setting $R_d = 4\Delta x$ is a reasonable choice in terms of accuracy and convergence properties both in 2D and in 3D and it is used for the simulations discussed in the following.

#### *4.2.1. Discussion on differences between 2D and the 3D dynamics*

The 3D ring evolution is shown in Fig. 8. The expected rising dynamics of the ring develops along with a decrease of the vorticity intensity of the ring core. In Fig. 9 the 3D evolution is compared with the 2D one in terms of vorticity fields. For the 3D solution, a section of the ring at $y = 0$ is shown.

As mentioned above, for the same simulation time the solutions are different, so that a comparison is carried out at times where the absolute vorticity maxima are the same vertical height. The 3D vorticity fields are in good agreement with the ones shown in [59] and in [63], where the same contour levels of Fig. 9 were adopted. The 3D solution appears less diffusive than the 2D one with a vorticity distribution generally more intense for the 3D case with respect to the corresponding 2D.

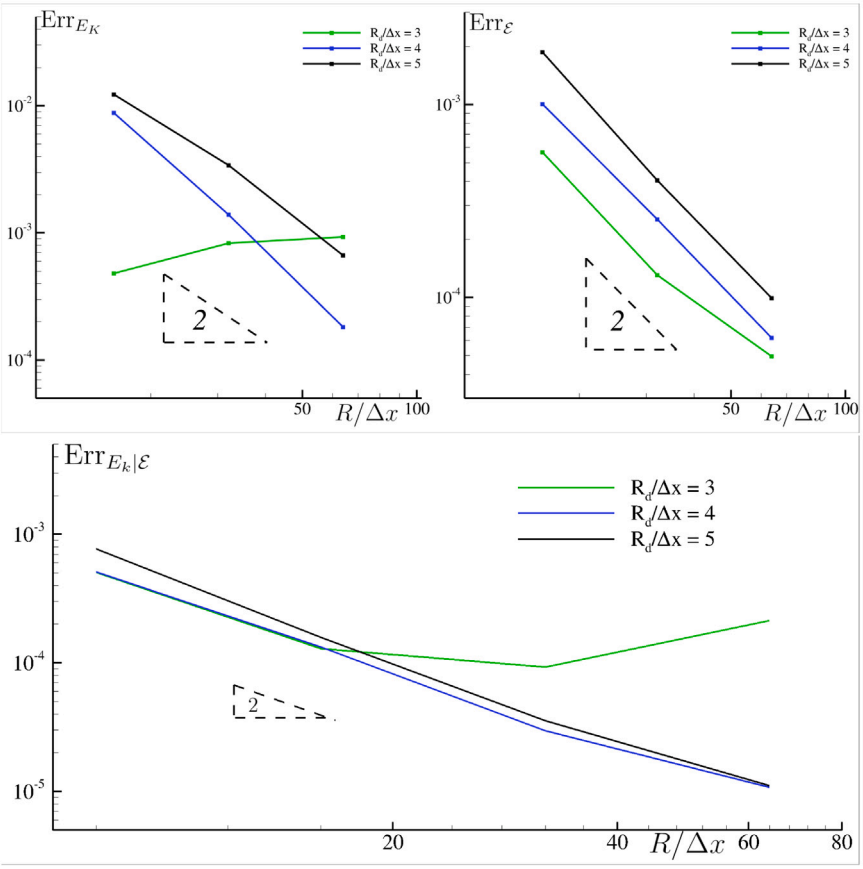


**Fig. 6.** **Top**: convergence of the $L^2$ norm between two subsequent resolutions for Energy (left) and Enstrophy (right) in 3D simulations for different values of $R_d$ and for resolutions up to $N = 64$. **Bottom**: convergence of energy–enstrophy conservation according formula (38) for different values of $R_d$ and for resolutions up to $N = 64$. Second order slope is also reported.

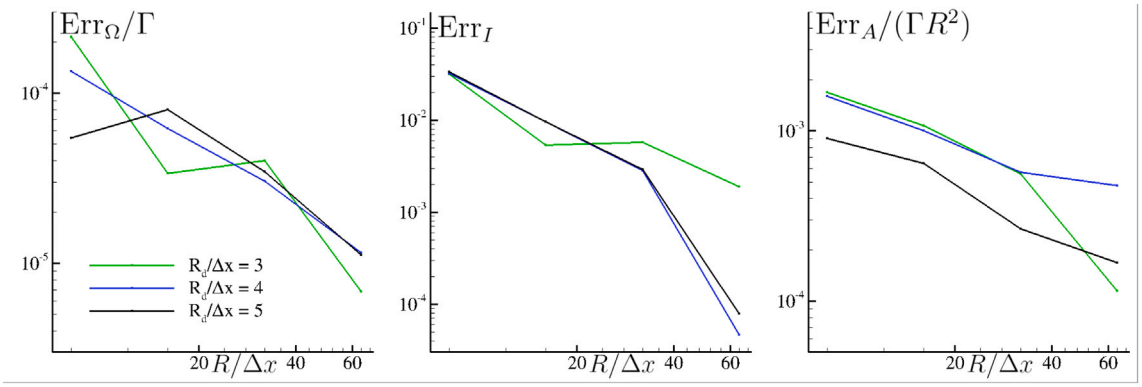


**Fig. 7.** Convergence of circulation (**left**), linear impulse (**middle**) and angular impulse (**right**) errors in 3D simulations at different diffusive radii and for resolution $N = 8, 16, 32, 64$. The circulation and the angular impulse errors, having no reference values, are made non-dimensional with $\Gamma$ and with $\Gamma R^2$, respectively.

The evaluation of the total circulation over the half-plane $y = 0$, $x < 0$ in 3D (over the half-plane $x < 0$ in 2D), hereinafter denoted as $\overline{\Gamma}(t)$, is reported in Fig. 10. This quantity is compared with the solution of Stanaway [59]. To this purpose, the time is made non-dimensional through $\bar{t} = t\ \nu^2/I_0$ in 3D and as $\bar{t} = t\ \nu^2/(RI_0)$ in 2D. The initial time is shifted to $\bar{t}_0 = 6.75 \times 10^{-5}$ in agreement with Stanaway [59]. The circulation is made non-dimensional with its initial value $\Gamma$. A very good agreement between the 3D solution and the reference one is achieved in terms of both slope and absolute values.

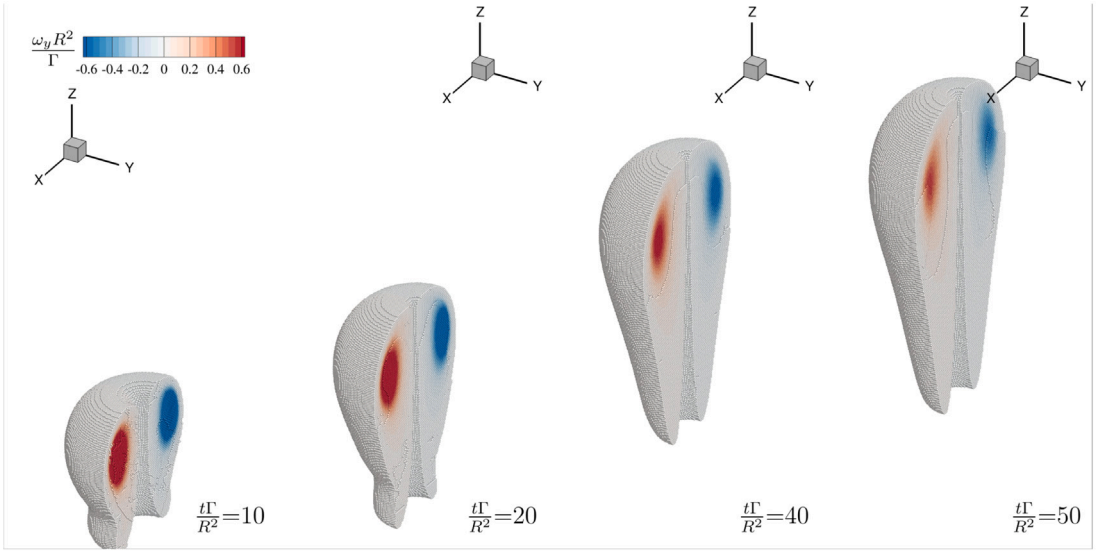


**Fig. 8.** 3D vortex ring evolution at $N = 32$ and $R_d = 4$. Ratio between diffusive and advective time steps is $N_{\Delta t} = 2$. Sections of the ring for $y/R < 0$ are shown. The reference non-dimensional time is indicated at bottom-right of each frame. Only particles with vorticity module $|\boldsymbol{\omega}_y R^2/\Gamma| > 1.5 \cdot 10^{-2}$ are shown.

The 2D solution, as explained above, evolves in a different time range and, for the same time instants, is characterized by larger values of the circulation than the 3D solution. This is due to the fact that the 3D ring is at a lower height than 2D dipole at same time instants. Following the same approach of Fig. 9, a comparison can be made when the ring and the dipole are at nearly the same height. For example, at $\bar{t} = 11.38$ (corresponding to $t\Gamma/R^2 = 40$) $\overline{\Gamma}$ is about 0.94 for 3D, whereas it is about 0.92 in 2D for $\bar{t} = 15.95$ ($t\Gamma/R^2 = 92$), so, as expected, at the same height the 2D solution possesses lower circulation than the 3D one (see corresponding times in Fig. 9).

Finally, a comparison between 2D and 3D simulations in terms of energy and enstrophy time behaviors is depicted in Fig. 11 for the maximum resolutions adopted ($N = 64$ for 3D, $N = 128$ for 2D). The quantities are normalized with their initial values, while the time is made non-dimensional with $\Gamma/R^2$. As visible, although the enstrophy decreases very similarly in both cases, the ring loses more energy in 3D than the dipole in 2D, when the same simulation time is considered. This reflects the behavior observed for the circulation in Fig. 10. Note that the initial energy in 3D is more than the double of the corresponding 2D one.

The is worth mentioning that the 2D simulation at $N = 128$ started with about 25,000 particles in the computational domain and ended at $t\Gamma/R^2 = 100$ with about 650,000 particles. Conversely, the 3D simulation at $N = 64$ started with 1.3 Million particles and ended at $t\Gamma/R^2 = 50$ with about 90 Million particles. From these numbers it is clear that an efficient parallel code is essential to perform 3D DVH simulations.

## 5. Conclusions

In the present paper, the PEPC-DVH 3D code is presented. The algorithm is a 3D extension of the DVH 2D code, a Vortex Particle Method introduced in [50] and widely validated during the last decade. The current algorithm is a new frontend of the open-source code PEPC, the *Pretty Efficient Parallel Coulomb solver*, which implements a highly portable, parallel Barnes–Hut tree code that was originally designed for mesh-free modeling of nonlinear, complex plasma systems [24,26]. With the new DVH frontend [16], it is used for a fast evaluation of the vortex particles' velocities.

The diffusion algorithm is based, similarly to the 2D code, on the superposition of heat equation simple solutions. The diffusion is carried out on a Cartesian lattice within a spherical area of radius $R_d$, which is the diffusive radius and is a parameter of the simulation.

In order to have stable simulations with the Chorin [9] fractional step method, diffusive and advective time steps must be synchronized. A useful criterion to get such a synchronization is described in Section 2.4, where the number of advective time steps before a diffusion step is defined. A general review of the conserved quantities has been given and some useful definitions in terms of Lagrangian particles are offered in Section 3.

A comparison between the 2D and the 3D code for the classic rising vortex ring test case [59] is in-depth investigated in Section 4. The 2D solution, defined as a vortex dipole corresponding to the 3D section of the ring, has been tested at increasing resolutions and the effect of different $R_d$ is evaluated. The convergence of kinetic energy and of enstrophy time histories have been studied, together with the conservation coming from the energy–enstrophy relation. A second order convergence has been observed and the value $R_d = 4\Delta x$ was found to be the best compromise between computational costs and accuracy.

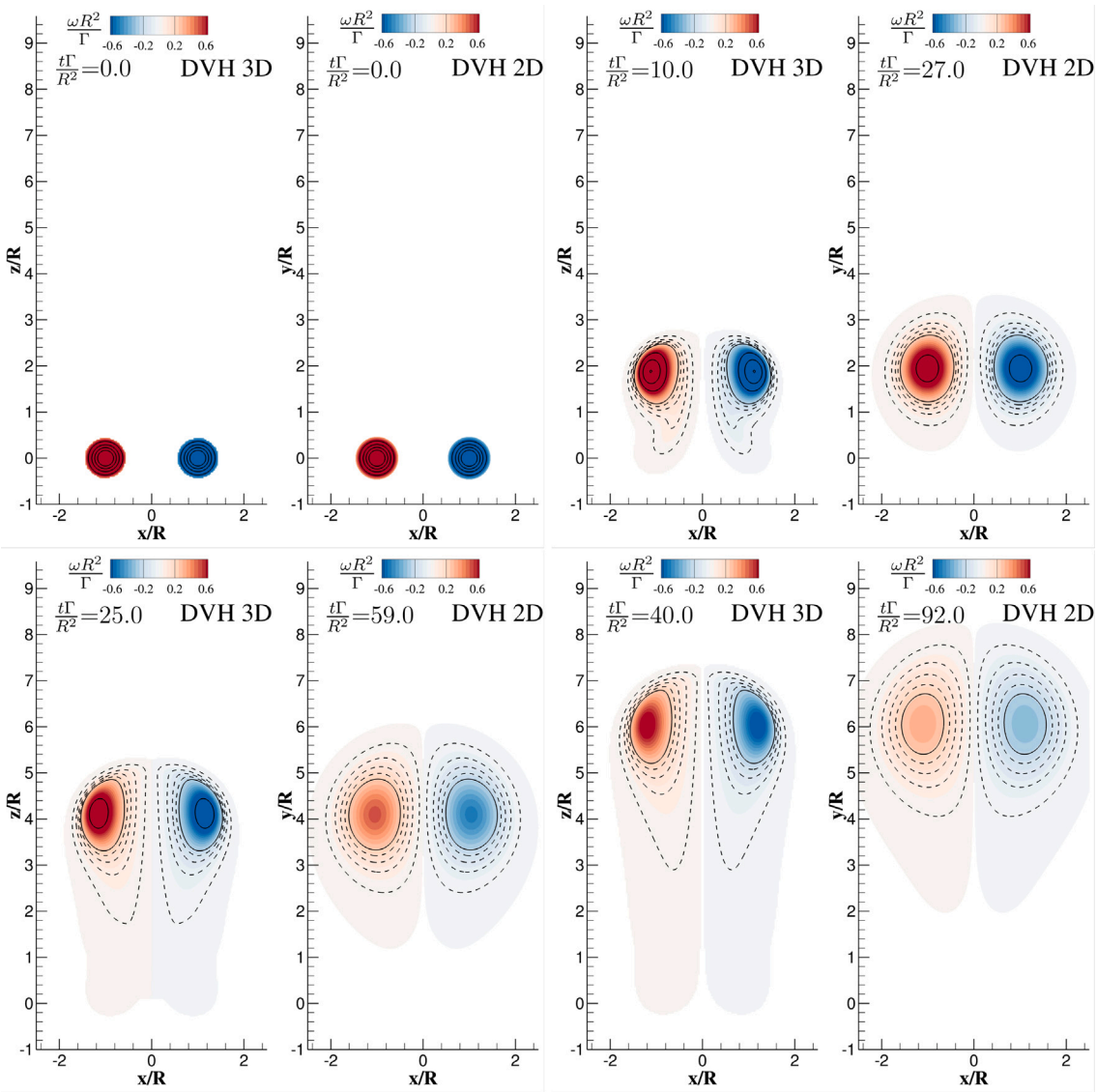


**Fig. 9.** 3D *vs.* 2D vortex ring evolution (contour map is indicated at the top). The particles with vorticity module $|\omega_y R^2/\Gamma| < 10^{-3}$ are blanked. The contour lines are referred to levels $0.024 \leq |\omega_y R^2/\Gamma| < 0.24$ with dashed lines and $0.24 \leq |\omega_y R^2/\Gamma| < 2.4$ with solid lines. Each interval is subdivided into 5 contour levels. The 3D solution is taken on the plane $y = 0$.

Similarly, the 3D solution was investigated for increasing resolutions and $R_d/\Delta x = 3, 4, 5$, confirming that $R_d = 4\Delta x$ is, even in 3D, an optimal choice for the diffusive radius. Convergence has been successfully verified for kinetic energy and enstrophy time histories and for the different integral momenta of the vorticity (total circulation, linear and angular impulse). A comparison with the solution by Stanaway [59] is carried out in terms of circulation evolution and a quite good agreement was found with the 3D DVH solution. This work represents a first milestone for this new algorithm and will be the basis for future developments and applications.

## CRediT authorship contribution statement

**D. Durante:** Conceptualization, Data curation, Formal analysis, Funding acquisition, Investigation, Methodology, Project administration, Resources, Software, Supervision, Validation, Visualization, Writing – original draft, Writing – review & editing. **S. Marrone:** Conceptualization, Data curation, Formal analysis, Investigation, Methodology, Software, Validation, Visualization, Writing – original draft, Writing – review & editing. **D. Brömmel:** Conceptualization, Project administration, Resources, Software, Supervision, Writing – review & editing. **R. Speck:** Funding acquisition, Project administration, Resources, Software, Supervision,

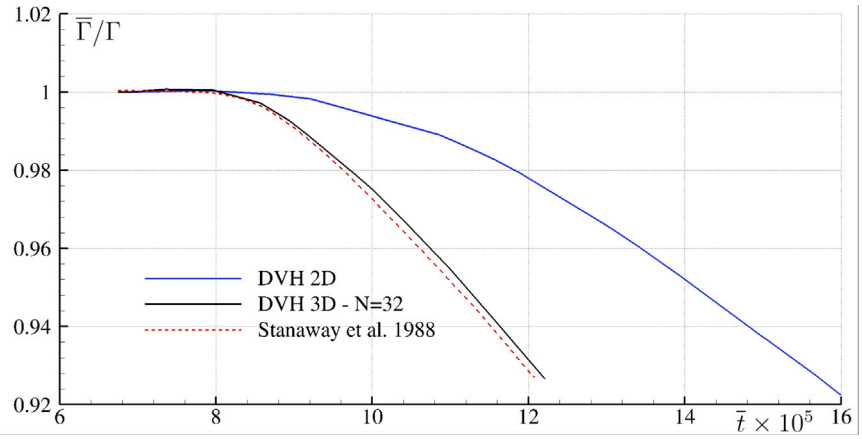


**Fig. 10.** Comparison of total circulation over a half-plane between 3D (black solid), 2D (blue solid) simulations and the solution of Stanaway [59] (dashed red). (For interpretation of the references to color in this figure legend, the reader is referred to the web version of this article.)

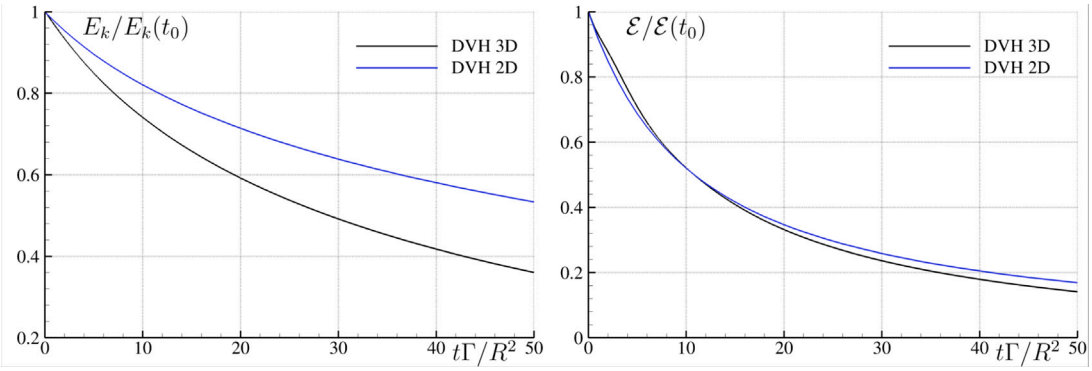


**Fig. 11.** Time histories of the kinetic energy (**left**) and enstrophy (**right**) for 2D and 3D simulations at maximum resolutions $N = 128$ and $N = 64$, respectively. Kinetic energy and enstrophy are normalized with their initial values: $E_k(t_0)/(\Gamma^2 R) = 0.55$ (3D), 0.26 (2D) ; $\mathcal{E}(t_0)R/\Gamma^2 = 9.96$ (3D), 3.25 (2D).

Writing – review & editing. **A. Colagrossi:** Conceptualization, Formal analysis, Methodology, Supervision, Writing – original draft, Writing – review & editing.

## Acknowledgments

We acknowledge the use of Fenix Infrastructure resources, which are partially funded from the European Union's Horizon 2020 research and innovation programme through the ICEI project under the grant agreement No. 800858. We also acknowledge the CINECA award `IscrC_DVH-3D` under the ISCRA initiative, for the availability of high performance computing resources and support. The present work was performed within the collaboration framework between Forschungszentrum Jülich (Jülich Supercomputing Center) and CNR-INM signed on 09/02/2024.

## Appendix. Inviscid convergence

By considering $L^p(\Omega)$, where $\Omega \subset \mathbb{R}^d$, as the Lebesgue space of locally *p-integrable* functions ($1 \leq p < \infty$), the Sobolev space $W^{m,p}(\Omega)$ is the space of functions $f \in L^p(\Omega)$ for which the weak $\beta-$th derivative $D^\beta f$ exists with $D^\beta f \in L^p(\Omega)$ and $|\beta| < m \in \mathbb{N}_0$.

**Theorem 1.** *Let $\zeta$ be a smoothing function of order $r \geq 2$ with core size $\epsilon > 0$ and*

$$\zeta \in W^{m,\infty}(\mathbb{R}^3) \cap W^{m,1}(\mathbb{R}^3) \qquad \forall m \in \mathbb{N}$$

*If the initial vorticity field $\boldsymbol{\omega}(\boldsymbol{x}, 0)$ is smooth enough and the initial particle spacing $h > 0$ is sufficiently small, then there exists a time $T > 0$ and a constant $C(T) > 0$ for which:*

$$\|(\boldsymbol{u} - \boldsymbol{u}_\epsilon)(\boldsymbol{x}, t)\|_{L^p(\mathbb{R}^3)} \leq C\epsilon^r \qquad \forall t \in [0, T] \ , \ p \in (3/2, \infty)$$

*if $h \leq B\epsilon^{1+s}$ for $s, B > 0$.*

**Proof.** The proof of the theorem can be found in [13].

## References


[1] E.J. Alvarez, A. Ning, Stable vortex particle method formulation for meshless large-eddy simulation, AIAA J. (2023) 1–20.
[2] L. Barba, A. Leonard, C. Allen, Numerical investigations on the accuracy of vortex methods with and without remeshing, in: 16th AIAA Computational Fluid Dynamics Conference, 2003, p. 3426.
[3] J. Barnes, P. Hut, A hierarchical O(N log N) force-calculation algorithm, Nature 324 (1986) 446–449.
[4] J.T. Beale, A. Majda, Rates of convergence for viscous splitting of the Navier–Stokes equations, Math. Comp. 37 (1981) 243–259.
[5] J.T. Beale, A. Majda, High order accurate vortex methods with explicit velocity kernels, J. Comput. Phys. 58 (1985) 188–208.
[6] J.V. Beck, K.D. Cole, A. Haji-Sheikh, B. Litkouhl, Heat Conduction using Green's Function, Taylor & Francis, 1992.
[7] M. Benson, P. Bellamy-Knights, J. Gerrard, I. Gladwell, A viscous splitting algorithm applied to low Reynolds number flows round a circular cylinder, J. Fluids Struct. 3 (1989) 439–479.
[8] A.J. Chorin, A numerical method for solving incompressible viscous flow problems, J. Comput. Phys. 2 (1967) 12–26.
[9] A.J. Chorin, Numerical solution of the Navier–Stokes equations, Math. Comput. 22 (1968) 745–762.
[10] A.J. Chorin, Numerical study of slightly viscous flow, J. Fluid Mech. 57 (1973) 785–796.
[11] A.J. Chorin, Vortex sheet approximation of boundary layers, J. Comput. Phys. 27 (1978) 428–442.
[12] A. Colagrossi, E. Rossi, S. Marrone, D. Le Touzé, Particle methods for viscous flows: Analogies and differences between the SPH and DVH methods, Commun. Comput. Phys. 20 (2016) 660–688.
[13] G. Cottet, P.D. Koumoutsakos, et al., Vortex Methods: Theory and Practice, Cambridge University Press, 2000.
[14] N. Didden, On the formation of vortex rings: rolling-up and production of circulation, Z. angew. Math. Phys. ZAMP 30 (1979) 101–116.
[15] D. Durante, O. Giannopoulou, A. Colagrossi, Regimes identification of the viscous flow past an elliptic cylinder for Reynolds number up to 10000, Commun. Nonlinear Sci. Numer. Simul. 102 (2021) 105902.
[16] D. Durante, S. Marrone, D. Brömmel, R. Speck, P. Gibbon, A. Colagrossi, The Pretty Efficient Parallel Coulomb solver (PEPC), 2024, URL: https://doi.org/10.5281/zenodo.10640946.
[17] D. Durante, C. Pilloton, A. Colagrossi, Intermittency patterns in the chaotic transition of the planar flow past a circular cylinder, Phys. Rev. Fluids 7 (2022) 054701.
[18] D. Durante, E. Rossi, A. Colagrossi, Bifurcations and chaos transition of the flow over an airfoil at low Reynolds number varying the angle of attack, Commun. Nonlinear Sci. Numer. Simul. (2020) 105285.
[19] D. Durante, E. Rossi, A. Colagrossi, G. Graziani, Numerical simulations of the transition from laminar to chaotic behaviour of the planar vortex flow past a circular cylinder, Commun. Nonlinear Sci. Numer. Simul. 48 (2017) 18–38.
[20] A.R. Edmonds, Angular Momentum in Quantum Mechanics, Princeton University Press, 1996.
[21] J.D. Eldredge, A. Leonard, T. Colonius, A general deterministic treatment of derivatives in particle methods, J. Comput. Phys. 180 (2002) 686–709.
[22] O. Giannopoulou, A. Colagrossi, A.D. Mascio, C. Mascia, Chorin's approaches revisited: Vortex particle method vs finite volume method, Eng. Anal. Bound. Elem. 106 (2019) 371–388.
[23] P. Gibbon, Pretty Efficient Parallel Coulomb-Solver, Technical Report. Technical report, Forschungszentrum Jülich GmbH, 2003.
[24] P. Gibbon, F.N. Beg, E.L. Clark, R.G. Evans, M. Zepf, Tree-code simulations of proton acceleration from laser-irradiated wire targets, Phys. Plasmas 11 (2004) 4032–4040.
[25] P. Gibbon, D. Brömmel, J. Chew, B. Steinbusch, M. Winkel, L. Siddi, R. Speck, L. Arnold, C. Salmagne, M.L. Henkel, M. Hofmann, H. Hübner, A. Breslau, M. Keldenich, The Pretty Efficient Parallel Coulomb solver (PEPC), 2023, URL: https://doi.org/10.5281/zenodo.7965549.
[26] P. Gibbon, R. Speck, A. Karmakar, L. Arnold, W. Frings, B. Berberich, D. Reiter, M. Mašek, Progress in mesh-free plasma simulation with parallel tree codes, IEEE Trans. Plasma Sci. 38 (2010) 2367–2376.
[27] P. Gibbon, M. Winkel, B. Steinbusch, R. Speck, D. Brömmel, L. Arnold, PEPC in the High-Q Club, 2013, URL https://www.fz-juelich.de/ias/jsc/high-q-club.
[28] V. Girault, P.A. Raviart, Finite Element Methods for Navier–Stokes Equations: Theory and Algorithms, Vol. 5, Springer Science & Business Media, 2012.
[29] O.H. Hald, Convergence of vortex methods for Euler's equations. II, SIAM J. Numer. Anal. 16 (1979) 726–755.
[30] O.H. Hald, Convergence of vortex methods for Euler's equations. III, SIAM J. Numer. Anal. 24 (1987) 538–582.
[31] T.Y. Hou, Convergence of a variable blob vortex method for the Euler and Navier–Stokes equations, SIAM J. Numer. Anal. 27 (1990) 1387–1404.
[32] T.Y. Hou, J. Lowengrub, Convergence of the point vortex method for the 3-D Euler equations, Commun. Pure Appl. Math. 43 (1990) 965–981.
[33] P.D. Koumoutsakos, G.H. Cottet, D. Rossinelli, Flow simulations using particles-bridging computer graphics and CFD, in: SIGGRAPH 2008-35th International Conference on Computer Graphics and Interactive Techniques, ACM, 2008, pp. 1–73.
[34] P. Koumoutsakos, A. Leonard, F. Pepin, Boundary conditions for viscous vortex methods, J. Comput. Phys. 113 (1994) 52–61.
[35] A. Leonard, Vortex methods for flow simulation, J. Comput. Phys. 37 (1980) 289–335.
[36] A. Leonard, Computing three-dimensional incompressible flows with vortex elements, Annu. Rev. Fluid Mech. 17 (1985) 523–559.
[37] D.G. Long, Convergence of the random vortex method in two dimensions, J. Amer. Math. Soc. 1 (1988) 779–804.
[38] A. Meldgaard, S. Darkner, K. Erleben, Fast vortex particle method for fluid-character interaction, in: Graphics Interface 2022, 2022.
[39] L.M. Milne-Thomson, Theoretical Aerodynamics, Courier Corporation, 1973.
[40] C. Mimeau, I. Mortazavi, A review of vortex methods and their applications: From creation to recent advances, Fluids 6 (68) (2021).
[41] A. Mokos, B.D. Rogers, P.K. Stansby, J.M. Domínguez, Multi-phase sph modelling of violent hydrodynamics on gpus, Comput. Phys. Comm. 196 (2015) 304–316.
[42] C. Oseen, Über die Wirbelbewegung in einer reibenden Flüssigkeit, Ark. Mat. Astro. Fys. (1912) 7.
[43] C. Rehbach, Numerical calculation of three-dimensional unsteady flows with vortex sheets, in: 16th Aerospace Sciences Meeting, 1978, p. 111.
[44] G. Riccardi, D. Durante, Elementi Di Fluidodinamica: Un'Introduzione Per L'Ingegneria, Springer Science & Business Media, 2007.
[45] L. Rosenhead, The formation of vortices from a surface of discontinuity, Proc. R. Soc. Lond. Ser. A Contain. Pap. Math. Phys. Charact. 134 (1931) 170–192.
[46] L. Rosenhead, The point vortex approximation of a vortex sheet, Proc. R. Soc. Lond. Ser. A Math. Phys. Eng. Sci. 134 (1932) 170–192.
[47] E. Rossi, 2D-Vorticity Genesis and Dynamics Studied Through Particle Methods (Ph.D. thesis), Citeseer, 2014.
[48] E. Rossi, A. Colagrossi, B. Bouscasse, G. Graziani, The diffused vortex hydrodynamics method, Commun. Comput. Phys. 18 (2015a) 351–379.
[49] E. Rossi, A. Colagrossi, D. Durante, G. Graziani, Simulating 2D viscous flow around geometries with vertices through the diffused vortex hydrodynamics method, Comput. Methods Appl. Mech. Engrg. 302 (2016) 147–169.
[50] E. Rossi, A. Colagrossi, G. Graziani, Numerical simulation of 2D-vorticity dynamics using particle methods, Comput. Math. Appl. 69 (2015b) 1484–1503.
[51] E. Rossi, A. Colagrossi, G. Oger, D. LeTouzé, Multiple bifurcations of the flow over stalled airfoils changing the Reynolds numbers, J. Fluid Mech. 846 (2018) 356–391.
[52] D. Rossinelli, M. Bergdorf, G.H. Cottet, P. Koumoutsakos, GPU accelerated simulations of bluff body flows using vortex particle methods, J. Comput. Phys. 229 (2010) 3316–3333.

[53] D. Rossinelli, B. Hejazialhosseini, W.van. Rees, M. Gazzola, M. Bergdorf, P. Koumoutsakos, Mrag-i2d: Multi-resolution adapted grids for remeshed vortex methods on multicore architectures, J. Comput. Phys. 288 (2015) 1–18.
[54] P.G. Saffman, The velocity of viscous vortex rings, Stud. Appl. Math. 49 (1970) 371–380.
[55] P.G. Saffman, Vortex Dynamics, Cambridge University Press, 1995.
[56] S. Shankar, L.Van. Dommelen, A new diffusion procedure for vortex methods, J. Comput. Phys. 127 (1996) 88–109.
[57] D. Shepard, A two-dimensional interpolation function for irregularly-spaced data, in: Proceedings of the 1968 23rd ACM National Conference, 1968, pp. 517–524.
[58] R. Speck, Generalized Algebraic Kernels and Multipole Expansions for Massively Parallel Vortex Particle Methods, Vol. 7, Forschungszentrum Jülich, 2011.
[59] S.K. Stanaway, A Numerical Study of Viscous Vortex Rings using a Spectral Method, Stanford University, 1988.
[60] J. Sweet, D.H. Richter, D. Thain, GPU acceleration of Eulerian–Lagrangian particle-laden turbulent flow simulations, Int. J. Multiph. Flow 99 (2018) 437–445.
[61] B. Wang, I. Wald, N. Morrical, W. Usher, L. Mu, K. Thompson, R. Hughes, An GPU-accelerated particle tracking method for Eulerian–Lagrangian simulations using hardware ray tracing cores, Comput. Phys. Comm. 271 (2022) 108221.
[62] M.S. Warren, J.K. Salmon, A portable parallel particle program, Comput. Phys. Comm. 87 (1995) 266–290, Particle Simulation Methods.
[63] D. Wee, A.F. Ghoniem, Modified interpolation kernels for treating diffusion and remeshing in vortex methods, J. Comput. Phys. 213 (2006) 239–263.
[64] G. Winckelmans, A. Leonard, Contributions to vortex particle methods for the computation of three-dimensional incompressible unsteady flows, J. Comput. Phys. 109 (1993) 247–273.
[65] M. Winkel, R. Speck, H. Hübner, L. Arnold, R. Krause, P. Gibbon, A massively parallel, multi-disciplinary barnes–hut tree code for extreme-scale n-body simulations, Comput. Phys. Commun. 183 (2012) 880–889.